JACS
JOURNAL OF THE AMERICAN CHEMICAL SOCIETY
Article
pubs.acs.org/JACS

Control of Plasmonic and Interband Transitions in Colloidal Indium Nitride Nanocrystals

Peter K. B. Palomaki, Elisa M. Miller, and Nathan R. Neale*

Chemical and Materials Sciences Center, National Renewable Energy Laboratory, 15013 Denver West Parkway, Golden, Colorado 80401, United States

Supporting Information

ABSTRACT: We have developed a colloidal synthesis of 4–10 nm diameter indium nitride (InN) nanocrystals that exhibit both a visible absorption onset (~1.8 eV) and a strong localized surface plasmon resonance absorption in the mid-infrared (~3000 nm). Chemical oxidation and reduction reversibly modulate both the position and intensity of this plasmon feature as well as the band-to-band absorption onset. Chemical oxidation of InN nanocrystals with $NOBF_4$ is found to red-shift the absorption onset to ~1.3 eV and reduce the plasmon absorption energy (to 3550 nm) and intensity (by an order of magnitude at 2600 nm). Reduction of these oxidized species with Bu_4NBH_4 fully recovers the original optical properties. Calculations suggest that the carrier density in these InN nanocrystals decreases upon oxidation from 2.89×10^{20} cm^{-3} to 2.51×10^{20} cm^{-3}, consistent with the removal of ~4 electrons per nanocrystal. This study provides a unique example of the ability to tune the optical properties of colloidal nanomaterials, and in particular the LSPR absorption, with reversible redox reactions that do not affect the semiconductor chemical composition or phase.

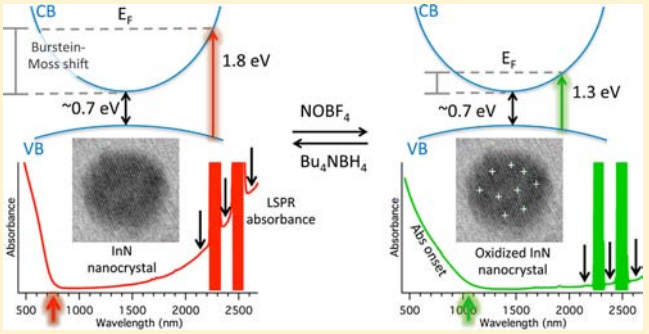

1. INTRODUCTION

Group III nitrides are an interesting and useful class of semiconductors owing to their direct band gaps, compositionally tunable optical properties, and large oscillator strengths. The band gap of group III nitride semiconductors ranges from the near-infrared (~0.7 eV for InN) to the ultraviolet (3.4 eV for GaN and 6.2 eV for AlN), making them well-suited for a variety of optoelectronic technologies.[1] For instance, GaN and gallium-rich InGaN materials comprise the active layer responsible for the tunable blue-to-green emission in high efficiency LEDs.[1] However, InN and indium-rich alloys of InGaN have not received the degree of attention paid to other group III nitride semiconductors, primarily owing to the challenges associated with their growth.[1−3] Recent progress in the preparation of high quality InN thin films resulted in the discovery that the band gap, originally reported to be ~2.0 eV for nonstoichiometric samples, had been grossly overestimated.[4] Only in the past decade has it become accepted that the band gap of InN is ~0.7 eV.[1−7] Given this discovery and the improvement in growth techniques, InN and indium-rich III-nitride alloys are receiving greater interest.[8] Recent studies have uncovered that InN exhibits a heavy effective hole mass and slow relaxation of hot carriers, properties that may be exploited for next-generation photovoltaic technologies based on hot carrier collection or multiple exciton generation.[1,9−11]

Interestingly, the previously observed absorption onset of ~2.0 eV is now known to be caused by indium surface states that introduce a large excess of free electrons into the bulk,[12,13] which moves the Fermi level above the conduction band minimum and results in a Burstein–Moss effect.[2,14] It has also been established that the high carrier density resulting from this self-doping gives rise to an intense plasmon absorption in InN thin films attributed to intraband transitions similar to that of a metal.[15] Materials exhibiting plasmon resonance features are under scrutiny for applications in telecommunications and optical tuning of plasmonic devices, for which the ability to tune the frequency and intensity of the plasmon for the application of interest is of critical importance.[16] Moreover, materials that combine both a semiconductor and a metal into a single (nano)structure are highly sought after for their ability to affect excited state electronic interactions.[17−20] Despite these promising characteristics, current understanding of the properties of InN nanostructures is lacking owing to the paucity of routes to well-defined material. Only a handful of reports have explored colloidal InN nanostructures, and none of these have demonstrated the ability to control and manipulate the photophysics of this semiconductor.[21−27]

The tuning of absorption features arising from a localized surface plasmon resonance (LSPR) in doped semiconducting nanostructures recently has been demonstrated in several nanostructured materials, including Sn-doped In_2O_3,[28,29] Al-doped ZnO,[30,31] oxygen-deficient tungsten oxides $WO_{3-\delta}$,[32] P-doped Si,[33] PbSe,[34] $Cu_{2-x}S/Se/Te$,[35−39] and $Cu_xIn_yS_2$,[40] and

Received: May 8, 2013
Published: August 24, 2013

   dx.doi.org/10.1021/ja404599g | J. Am. Chem. Soc. 2013, 135, 14142−14150

has been reviewed elsewhere.[41] Controlling the position and intensity of the LSPR absorbance feature most commonly has been achieved by adjusting the doping density of semiconductor nanocrystals (NCs),[30,32,33,38,39] though other strategies to affect the LSPR include electrochemical (Sn-doped In_2O_3[28] and PbSe[34]), size manipulation ($Cu_{2-x}S$),[40] and chemical treatments ($Cu_{2-x}S$/Se/Te),[36,37] the last of which additionally alter the stoichiometry of the NCs. In contrast to the solution-phase modulation of LSPRs in metal chalcogenide semiconductors using chemical redox reagents, the more covalent bonding nature in InN affords the possibility of dynamically modifying the charge carrier density without altering its chemical composition.

Herein, we report the reversible tuning of LSPRs in colloidal InN NCs using simple redox chemistry. As-prepared samples contain a large excess of free electrons, which moves the Fermi level above the conduction band minimum such that two optical characteristics are evident: a Γ−Γ band transition well in excess of the band gap owing to the Burstein−Moss effect as well as an intense LSPR feature. To control the photophysical properties of this material, we chemically oxidized the NCs to decrease the free carrier density as evidenced by a reduced intensity and lower energy LSPR. Concomitantly, a significant shift in the absorption onset from ∼1.8 to ∼1.3 eV is observed, indicating that the Fermi level moves closer to the conduction band minimum upon oxidation. We also show that this oxidation is reversible, with the original absorption properties recovered upon chemical reduction. To the best of our knowledge, this example is the first observation of control of the carrier density of colloidal InN NCs and, more generally, this strategy of chemical redox reactions affords a pathway to tune the carrier density of related colloidal nanoscale semiconductors where changes in semiconductor stoichiometry are undesirable (e.g., photovoltaics).

2. EXPERIMENTAL SECTION

All solvents were purchased from Aldrich or Fischer, ACS grade or better unless otherwise noted. Reactions were performed in a nitrogen-filled glovebox or on a Schlenk line under positive nitrogen pressure. In_2S_3 (Alfa Aesar, 99.98%), $NaNH_2$ (Sigma Aldrich, 98%), Et_3OBF_4 (Fluka, ≥97%, stored in glovebox), $NOBF_4$ (Fluka, ≥98%, stored in glovebox), Bu_4NBH_4 (Sigma Aldrich, 98%, stored in glovebox), oleylamine (OAm, Sigma Aldrich, tech grade, 70%), ethanol (absolute), acetonitrile (ACN), toluene, chloroform, tetrachloroethylene (TCE), dimethylformamide (DMF), and hexanes were used as received unless otherwise noted. Octadecene (Sigma Aldrich, technical grade, 90%) was degassed and dehydrated overnight at 100 °C under dynamic vacuum (∼10 mTorr) before being transferred to and stored in the glovebox. Anhydrous acetonitrile was purified by distilling from calcium hydride under nitrogen.

2.1. Synthesis of InN Nanocrystals. Under inert atmosphere, In_2S_3 (81.5 mg, 0.25 mmol) and $NaNH_2$ (97.5 mg, 2.5 mmol) were combined with octadecene (2.5 g) in a vial with a PTFE lined rubber sealed cap and a stir bar. The mixture was stirred and heated on a hot plate with an aluminum heating block in a glovebox to 100 °C. The temperature was increased at a rate of 5−10 °C/min until the desired reaction temperature was reached. After the reaction temperature was held for 15 min to 12 h, the mixture was cooled to room temperature and then removed from the glovebox. Workup was performed in ambient atmosphere. The black solid was washed with 10−20 mL of hexanes, 10−20 mL of ethanol, 10−20 mL of deionized water, and finally 20−30 mL of ethanol. At each step, the suspension was shaken or sonicated to ensure complete dissolution of organic solvent or byproducts. The resulting black-brown solid (containing a mixture of InN/In^0) was sonicated with nitric acid (∼4 vol % aqueous, 3−5 mL) for 3−5 min to remove In^0 before centrifugation followed by washing with ethanol (5−10 mL). Oleylamine (2−5 mL) was then added, and the dark brown mixture was alternated between sonication and heating at ∼95 °C for 20−60 min or until most material had dissolved. The addition of toluene (2−5 mL) assisted in dissolving most material. Typically the smaller sized particles (shorter reaction times and lower temperature reactions) dissolved more readily while the larger particles required extended heating and sonicating. Particles were precipitated from the oleylamine/toluene mixture with ethanol (20−30 mL) and dissolved in toluene or hexanes (1−5 mL) before a second precipitation with ethanol (10−30 mL) was performed. The resulting brown solid was soluble in nonpolar solvents such as toluene, hexanes, chloroform, and tetrachloroethylene. A color change from black to brown was observed following the postsynthesis washing procedure, most likely due to removal of In^0, byproducts, and other impurities from the reaction.

Size-selective precipitation was performed by dissolving OAm-capped InN NCs in 3−5 mL of toluene and adding ACN dropwise (<1 mL) while stirring. Upon observation of a precipitate the mixture was centrifuged and the supernatant solution decanted. To the supernatant was added <1 mL of ACN dropwise until observation of a precipitate. This solid was collected by centrifugation and analyzed by TEM. Earlier fractions showed a larger average size. Polydispersity could be further narrowed by repetition of this procedure.

Films of insoluble samples (prior to attachment of ligand) were dispersed in ethanol and drop-cast onto a glass substrate at 80 °C, whereas those of OAm-capped samples were drop-cast from a compatible solvent (e.g., toluene, 9:1 (v/v) hexanes/1-octene) onto a glass substrate for XRD analysis or a 1 mm thick Si window (Edmund Optics no. 68-523) for FTIR.

2.2. Nanocrystal Surface Treatments. A solution of Et_3OBF_4 was prepared by dissolving ∼40 mg of Et_3OBF_4 in 1 mL of DMF. The Et_3OBF_4 solution was added to a solution of ∼10 mg InN NCs in hexanes (2−3 mL). The mixture was shaken for ∼1 min before adding toluene (15−20 mL). The mixture was centrifuged and the resulting solid dissolved in ACN (2−5 mL) and precipitated again with toluene (15−20 mL). After a final centrifugation, the solid was dissolved in ACN for optical characterization or film deposition.

Solution spectra of $NOBF_4$-treated NCs were obtained by adding a saturated solution of $NOBF_4$ in ACN (made by sonicating >20 mg of $NOBF_4$ in 2−3 mL of ACN) dropwise to a solution of Et_3OBF_4-treated NCs in ACN (∼1 mg/mL) in a cuvette until no further change in the absorbance spectra was observed. Subsequent reduction was performed by addition of a solution of Bu_4NBH_4 (∼0.033 mM in ACN) dropwise to the cuvette.

Films of $NOBF_4$-treated NCs were obtained by adding ∼0.5 mL of a saturated solution of $NOBF_4$ in ACN to 1 mL of a solution of InN NCs in hexanes (5−20 mg/mL). The mixture was shaken and sonicated to ensure complete reaction, then precipitated with toluene. Following centrifugation, the solid was dissolved in ACN and a film was drop-cast from ACN (5−20 mg/mL) for FTIR analysis.

2.3. Characterization. X-ray diffraction (XRD) was performed on a Rigaku D/MAX 2500H goniometer (with 185 mm radius) using a Cu Kα radiation (0.154 06 nm) line source generated with an UltraX-18 rotating anode at 40 kV and 250 mA in a Bragg−Brentano configuration. The sample was mounted onto a vertical stage and continuously scanned from 25°−55° 2θ using 0.02° bins at 0.5°/min. The X-ray beam was height-limited to 10 mm and conditioned with a 2/3° divergence slit and received with a 1/6° scatter and 0.15 mm receiver slits. Both source and receiving optics also had 5° Soller slits. The scattered X-rays were detected with a scintillation counter after passing through a single-bounce graphite monochromator. Diffraction lines are compared to JCPDS card numbers as follows: 00-002-145 (InN), 00-005-0642 (In^0), 00-005-0731 (In_2S_3), 00-006-0416 (In_2O_3), 00-023-0441 (Na_2S), and 00-035-1186 ($NaInS_2$).

TEM images were obtained on a Philips/FEI CM200 with a LaB_6 filament operating at 200 keV. Samples were prepared by allowing one drop of a dilute solution of nanoparticles in chloroform or hexanes to evaporate on an ultrathin carbon on holey support TEM grid (400 mesh, Ted Pella no. 01824). Size measurements were made using ImageJ software where at least 100 particles were counted from

multiple images. Measurements of the diameter of nonspherical NCs were made along a vertical line (with respect to the image orientation) through the center of the NC for consistency.

UV−vis−NIR measurements were obtained on a Varian Cary 500 spectrophotometer from 3300 to 400 nm in 1 or 2 nm increments at a rate of 600 nm/min with a bandwidth of 2 nm. Solution spectra were obtained in TCE (OAm-capped samples) and ACN (Et_3OBF_4- and $NOBF_4$-treated samples).

FTIR measurements were performed on InN NC films on a Si window using a Thermo Nicolett 6700 from 6000 to 650 cm^{-1} at a resolution of 4 cm^{-1} for 64 scans. Background spectra were obtained on a clean Si window of the same type. Emission experiments were conducted at room temperature on films of NCs on a quartz substrate using the reflectance mode in a modified Horiba Jobin-Yvon Fluorolog 3 fluorescence system (model FL3-2IHR). Excitation at 420 nm was accomplished by a 450 W xenon lamp, with wavelength selection provided by a double-grating spectrometer (grating specs, 1200 grooves/mm, blazed at 500 nm), and fluorescence from the samples was detected with a liquid-nitrogen-cooled CCD detector coupled to a single-grating iHR320 imaging spectrometer (grating specs, 150 grooves/mm, blazed at 500 nm). All spectra were corrected for the response of the detection system.

Elemental analysis (EA) for indium, nitrogen, sulfur, and boron was performed by Huffman Laboratories (Golden, CO). Indium, sulfur, boron, and fluorine content was determined by inductively coupled plasma optical emission spectroscopy, and nitrogen was determined by the Dumas method. All analyses were performed in triplicate and averaged.

X-ray photoelectron spectroscopy (XPS) experiments were performed on a PHI 5600 photoemission spectrometer using Al Kα (1486.6 eV) X-rays, which has been previously described.[42] High-resolution spectra were obtained under ultrahigh vacuum conditions (10^{-10} Torr) with a pass energy of 29.35 eV and a step size of 0.125 eV. The energy scale was calibrated with known Au $4f_{7/2}$ and Cu 3p and $2p_{3/2}$ core-level energies. Films for XPS were spin coated from DMF (20−100 mg/mL) on oxygen plasma cleaned gold substrates. None of the films exhibited charging during the XPS experiments.

3. RESULTS AND DISCUSSION

Indium nitride NCs used in this study were prepared from the reaction of indium sulfide (In_2S_3) with sodium amide ($NaNH_2$) in octadecene at atmospheric pressure, an adaptation from a literature report using a high-pressure solvothermal route.[21] As-prepared samples contain metallic indium metal (In^0) by-product as evidenced by XRD (Figure 1), consistent with the byproduct formed from reactions of indium precursors and amide at atmospheric pressure.[21,24,26] Using the method developed by Hseih et al.,[26] In^0 was removed by washing with dilute nitric acid as evidenced by the lack of In^0 reflections in the XRD spectrum (Figure 1). Notably, the InN peak position and full width at half-maximum remain similar both before and after acid treatment, suggesting that the InN NC size is not significantly affected by the metal etch. Consistent with these XRD results, TEM analyses of the samples before In^0 removal reveal what appears to be a network of In^0 surrounding the InN NCs (Figure 2a) that is removed by the acid etch, leaving network-free, agglomerated InN NCs (Figure 2b). Hydrophobic InN NCs soluble in nonpolar solvents were prepared by gently heating the agglomerated NCs in excess OAm at ∼95 °C for 20−40 min (Figure 2c). Though these surface-functionalized InN NCs are relatively polydisperse (24−38%), Figure 2d shows that fractions can be isolated with <20% polydispersity via a single size-selective precipitation step (for size histograms, see Figure S1). Attempts to functionalize the InN NCs with oleic acid, dodecanethiol, trioctylphosphine, and trioctylphosphine oxide do not result in hydrophobic solvent-soluble material, suggesting that these ligands do not coordinate well to the InN NC surface.

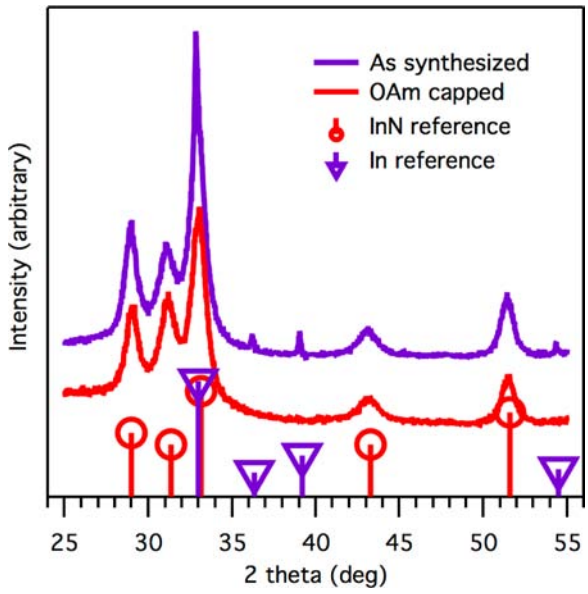

Figure 1. X-ray diffraction spectra of the as-synthesized InN/In^0 product (red) and following In^0 removal and capping with OAm (blue, offset for clarity). Once treated with nitric acid and functionalized with OAm, the In^0 diffraction peaks at 33.0° (obscured with InN peak), 36.2°, 39.2°, and 54.4° are no longer present, suggesting that In^0 has been fully removed.

Control of InN NC size below the exciton Bohr radius (8 nm) would be expected to begin to change the optical properties owing to quantum confinement. Previous reports on the synthesis of colloidal InN NCs have not demonstrated tunable sizes below 10 nm where quantum confinement effects become important.[21−26] In the method developed here, we found that changing the reaction time and temperature were both successful in controlling the InN NC diameter in this small size regime. Increasing the reaction time (Figure 2e, blue circles) from 15 min to 12 h results in NCs with average sizes ranging from 4.5 to 9.9 nm (temperature for these reactions was held constant at 220 °C). Longer reaction times beyond 12 h do not significantly increase the NC size. Adjusting the reaction temperature between 175 and 200 °C (Figure 2e, red squares) provides NC sizes ranging from 4.1 to 8.0 nm (time for these reactions was 3 h), whereas temperatures below 175 °C do not produce InN as evidenced by XRD (Figure S5). The observation of crystalline InN at reaction temperatures of at least 175 °C agrees well with the proposed mechanism for reactions between indium precursors and amide in which an $In(NH_2)_3$ intermediate decomposes to InN near this temperature.[43]

Additional increases in reaction temperature above 200 °C do not result in any statistical increases in NC size. All InN NCs used for optical studies (vide infra) were synthesized at 220 °C for 30 min, resulting in a 6.0 ± 2.2 nm particle diameter.

A Tauc plot of UV−vis−NIR absorbance data from a solution of 6.0 ± 2.2 nm diameter OAm-capped InN NCs in tetrachloroethylene (TCE) is shown in Figure 3 (blue trace) and confirms that the abrupt rise in the visible absorbance is a direct transition with an absorption onset value of 1.81 eV. As noted above, this optical feature does not result from band gap excitation (expected at ∼0.7 eV for bulk InN) but instead is due

dx.doi.org/10.1021/ja404599g | J. Am. Chem. Soc. 2013, 135, 14142−14150

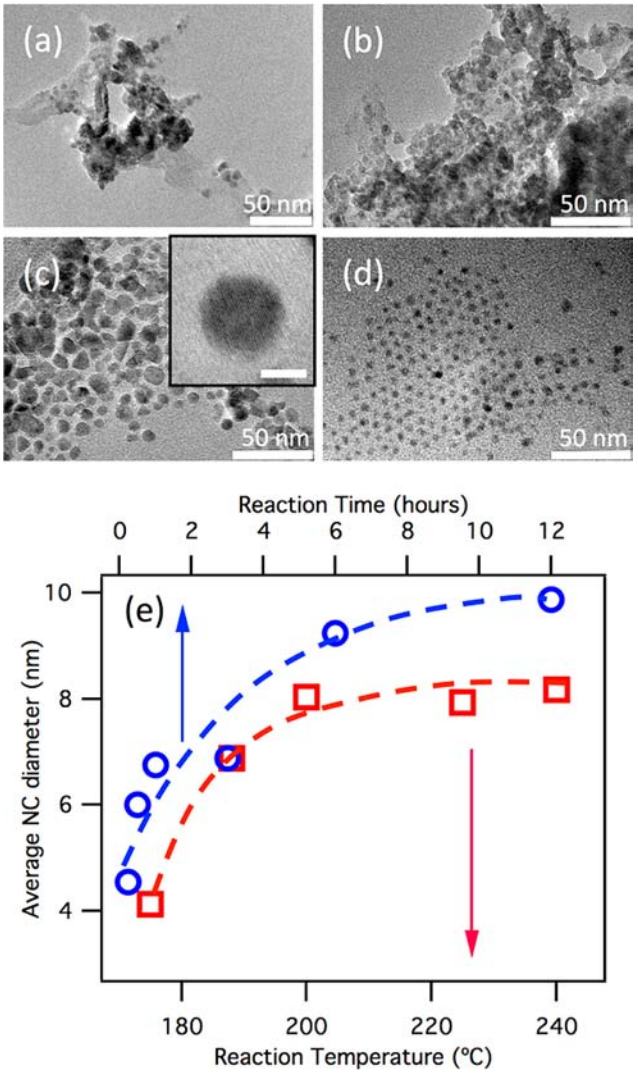

Figure 2. TEM images of InN NCs: (a) as-synthesized InN NCs bound in an In^0 matrix; (b) agglomerated particles following dissolution of In^0 with HNO_3; (c) free-standing NCs after surface functionalization with OAm ligands (inset scale bar, 5 nm); (d) a size-purified fraction. (e) Plots of average size of InN NCs at varying reaction times (blue circles, constant temperature of 220 °C) and varying reaction temperatures (red squares, constant time of 3 h). Dashed lines in (e) are guides to the eye.

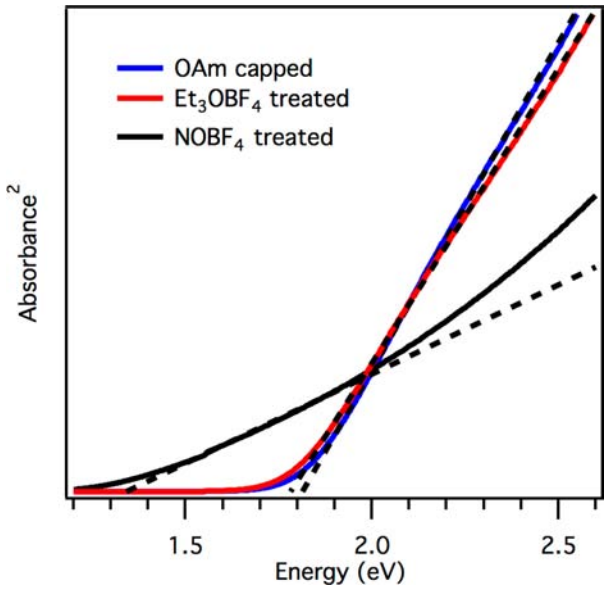

Figure 3. Tauc plots of 6.0 nm InN NCs with as-prepared OAm ligands, following ligand exchange with Et_3OBF_4 and upon oxidation with $NOBF_4$. Dashed lines are fits to the linear regions of the curves with the *x*-intercept taken as the absorption onset. No significant changes in optical properties are observed upon ligand exchange from OAm to BF_4^-, but a clear shift in the absorption onset is observed from ~1.8 to ~1.3 eV upon oxidation with $NOBF_4$.

to a higher energy excitation pathway. It has been proposed that surface states inject significant electron density into the semiconductor, which effectively dopes the material and leaves it with a high free carrier density.[12] This high free carrier density pushes the Fermi level above the conduction band minimum, resulting in band-to-band transitions that are much higher in energy than the band gap (the Burstein–Moss effect).[2,14] We thus assign the red-visible optical absorption onset to a Γ–Γ band transition exhibiting a significant Burstein–Moss shift that is in agreement with prior reports of similar transitions in both bulk[2,14] and nanocrystalline[26] InN.

In addition to the interband transition in the red-visible region (Figure 4a, black trace), the sample also exhibits a strong, broad absorption feature that extends well into the IR region of the spectrum with a maximum at ~3000 nm (0.41 eV) (Figure 4a, red trace). A previous report also showed InN NCs with dramatically increasing absorbance between 0.9 and 0.5 eV and attributed this feature to Urbach band tails.[26] Given that these tails are typically associated with transitions from an exponential decay of mid-gap states to localized band states (or vice versa), the number of these states are insignificant compared with that of extended state (band-to-band) transitions.[44] Thus, the assignment of such a strong transition as an Urbach tail would appear to be inconsistent with the IR absorbance feature observed here that is comparable in intensity to the interband absorption ascending into the visible region. We propose that the strong IR absorption feature in these InN NC samples results from a localized surface plasmon resonance (LSPR). Strong plasmon absorption due to high carrier density has been observed in thin film InN [15,45] but to the best of our knowledge has not been ascribed previously to InN NCs. Absorbance spectra in different solvents confirm that this absorption feature is in fact due to a LSPR based on the observation of a red shift with increasing solvent refractive index and a refractive index sensitivity value of 284 nm/RIU (Figure S10).

As noted above, tuning the LSPR is of interest for a variety of optoelectronic and imaging applications. For the self-doped InN NCs under investigation here, oxidation should result in a decrease in the carrier density and a concomitant reduction of the Fermi level, resulting in a lower intensity, red-shifted plasmon absorbance. We first treated OAm-capped InN NCs with Meerwein's salt (Et_3OBF_4), which has recently been shown to strip amine ligands (as well as others) from a variety of NC species without significantly changing the semiconductor electronic properties.[46] This treatment provides a bare NC surface with weakly coordinated BF_4^- ligands as well as imparting solubility in polar solvents.

Both the absorption onset and the plasmon absorption feature undergo minmal change upon ligand exchange, suggesting that the NCs are not oxidized and the carrier density is not significantly affected by the ligand exchange

dx.doi.org/10.1021/ja404599g | J. Am. Chem. Soc. 2013, 135, 14142–14150

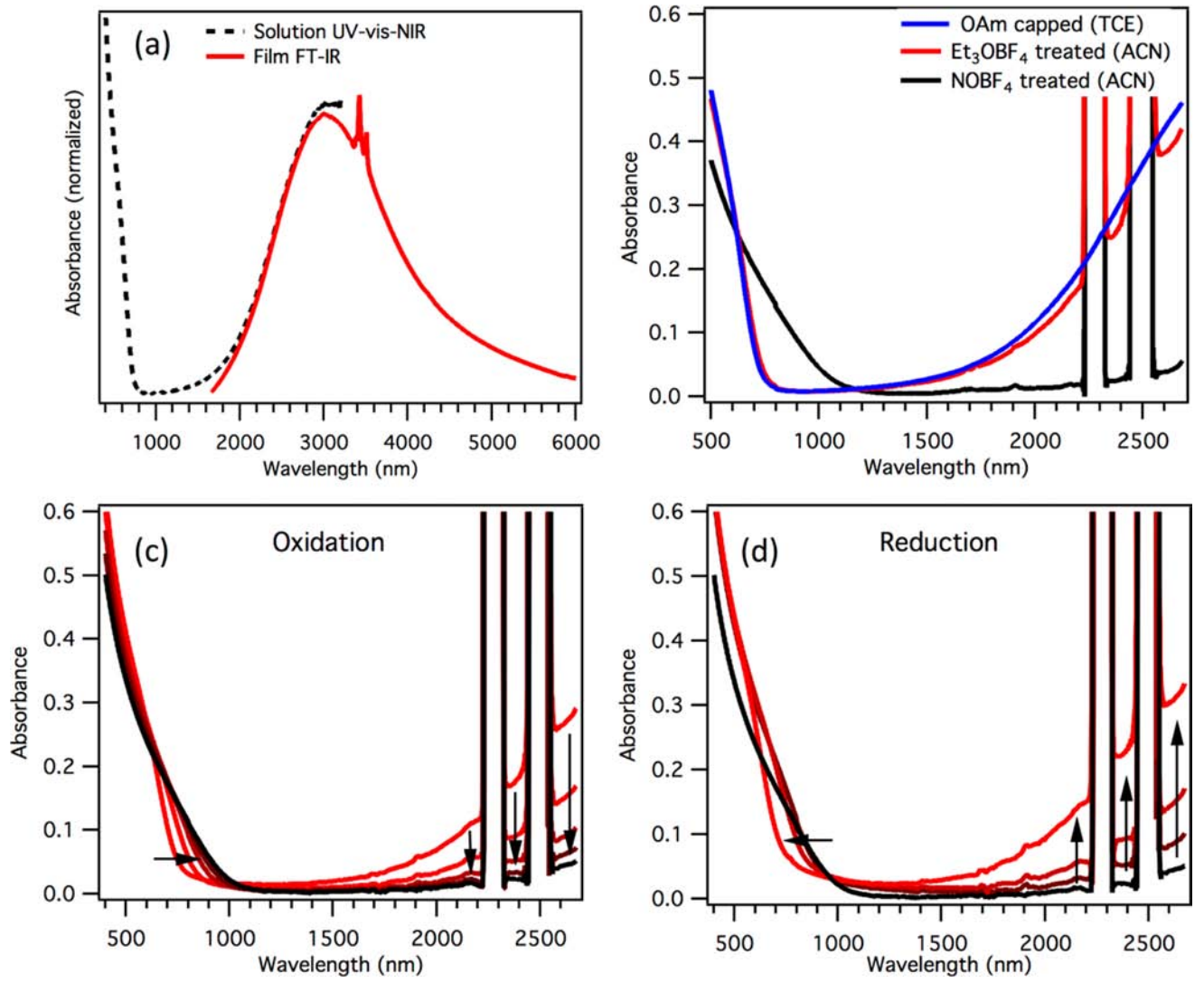

Figure 4. UV−vis−NIR absorption spectra of (a) 6.0 ± 2.2 nm OAm-capped InN NCs in tetrachloroethylene solution (black dashed trace) and the FTIR spectrum of a film of the same sample (red solid trace) showing the expected vibrations from oleylamine (OAm) ligands along with a broad, intense feature attributed to a localized surface plasmon resonance that is of comparable intensity to the absorption onset in the red-visible region, (b) as-prepared InN NCs with OAm ligands (blue), following ligand exchange with Et_3OBF_4 (red) and upon oxidation with excess $NOBF_4$ (black), stepwise (c) oxidation and (d) subsequent reduction of a InN NC solution in ACN showing reversible and tunable optical transitions owing to a change in carrier density. The spectra in (c) were obtained from a solution of Et_3OBF_4-treated InN NCs in ACN treated with 0, 1, 3, 5, and 10 drops of saturated $NOBF_4$ solution (red to black). The spectra in (d) were obtained by treating the solution containing 10 drops of $NOBF_4$ solution with 0, 10, 15, and 20 drops of 33 μM Bu_4NBH_4 (black to red). Arrows indicate the direction of change in the spectra upon chemical redox.

process (Figure 4b). This observation is consistent with the thesis recently proposed by Helms and co-workers that trialkyloxonium salts are mild, universal reagents for control of NC surface chemistry without impacting their photophysics.[46]

To effect a change in the carrier density (and photophysics), BF_4^--capped InN NCs were chemically oxidized using the strong oxidant nitrosonium tetrafluoroborate ($NOBF_4$).[47] This reagent has been used to exchange the head-to-tail ligands OAm and oleate with BF_4^- to provide polar solvent-soluble $NaYF_4$ NCs, though in the prior report no oxidation was observed owing to quenching of the nitrosonium cation by ambient water.[48] In the aprotic solvent used here (ACN), $NOBF_4$ oxidizes the InN NCs, as evidenced by the absorption onset shift to >1000 nm and the drastic intensity decrease in the near-infrared LSPR (Figure 4b). These absorbance changes are consistent with a reduction in the free carrier density and lower energy transitions from the valence band to the Fermi level indicative of a decreased Burstein−Moss shift as described by the cartoon in Figure 5. The 1.34 eV absorption onset obtained from a Tauc plot of the absorbance data from this oxidized sample (Figure 3) is the lower limit achieved via oxidation using excess $NOBF_4$; it is important to note that treatment of the NCs with lower oxidant concentrations provides stepwise changes to both the absorption onset and the LSPR intensity (Figure 4c). Therefore, fine-tuning of the absorption onset over the range 1.8−1.3 eV and the LSPR to a fraction of its original intensity (e.g., 10% at 2600 nm) is possible using this redox chemistry approach.

The fact that an oxidation limit is achieved with $NOBF_4$ agrees with the observation that no emission is detected for InN NC films (for OAm-capped, BF_4^--exchanged, or $NOBF_4$-oxidized NCs), which might be expected once the NCs are sufficiently oxidized to push the Fermi level to an energy lower

dx.doi.org/10.1021/ja404599g | J. Am. Chem. Soc. 2013, 135, 14142−14150

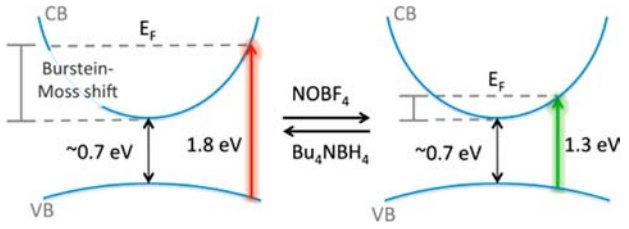

Figure 5. Depiction of changes to the interband transition energies in InN NCs upon redox chemistry with $NOBF_4$ and Bu_4NBH_4. Once oxidized, electrons are removed from the conduction band and the Burstein–Moss shift decreases resulting in a lower-energy transition. Chemical reduction recovers the original carrier density and optical properties.

than the conduction band minimum but not before. The absence of emission at 650 nm (1.9 eV) also suggests that all samples lack oxygen related defects for which emission has been previously observed.[3] The oxidation limit resulting in an absorption onset at 1.3 eV is achieved regardless of the NC size, confirming that the limit is not associated with a reduced band gap owing to quantum confinement.

Changes in chemical composition upon InN NC ligand exchange and oxidation were explored by EA and XPS. The results shown in Table 1 demonstrate that for as-prepared,

Table 1. Elemental Ratios from EA and XPS[a]

	EA results		XPS results	
surface treatment	In/N	In/S	In/N	In/S
OAm			1.09	3.4
Et_3OBF_4	1.25	2.4	1.98	3.3
$NOBF_4$	1.45	6.9	1.92	6.9

[a]Standard deviation from triplicate measurements of EA is ±0.01 and ±0.05 for In/N and In/S, respectively.

OAm-capped InN NCs the In/N is 1.09:1 via XPS analysis. However, given that the OAm ligand also contributes to the nitrogen content, the In/N ratio within the semiconductor should be greater than this value. Consistent with this supposition, removal of the OAm ligands using Et_3OBF_4 increases the In/N ratio to 1.25 (EA) and 1.98 (XPS). In/N ratios of 1.45 (EA) and 1.92 (XPS) were found for samples oxidized with $NOBF_4$. The apparent discrepancies between the In/N ratios from EA and XPS could result from two effects: (1) an increased sensitivity of XPS to the surface and near surface species, which may contain higher proportions of indium, and (2) the presence of surface-adsorbed DMF, which would contribute to N-content in EA but would be desorbed in the ultrahigh vacuum conditions of XPS. Consistent with this latter hypothesis, the EA results show an increased In/N ratio upon oxidation with $NOBF_4$, which is expected from DMF desorption owing to additional charge-balancing BF_4^- ions at the NC surface. Further evidence is provided from EA and XPS analyses which show an increase in fluorine and boron content upon oxidation (Table S3), which we attribute to more surface-associated BF_4^- ions. In addition, both EA and XPS analyses are consistent with respect to excess metal content, a phenomenon commonly found in colloidally grown, binary semiconductor NCs such as CdSe,[49] PbSe,[50] and InN.[21,24,26] Whereas the photophysics of metal chalcogenide NCs may be tuned by varying the stoichiometry at the NC surface,[51−53] this strategy has not been demonstrated for InN NCs. Modifying the chemical composition of these metal-rich InN NCs via surface chemistry modification may afford another avenue to tune the optical properties of this material.

Intriguingly, a more unexpected finding suggests that surface chemistry modification does change the chemical composition of the NC surface. In contrast to XRD data showing minimal changes in the InN peak positions and shapes, and the absence of In^0, In_2O_3, In_2S_3, or other reflections of InN NCs after oxidation with $NOBF_4$ (Figure S11), suggesting that the NCs are predominantly crystalline InN with minimal crystalline impurities, EA and XPS analyses demonstrate the presence of spectroscopically inactive sulfur species in the InN NC samples, presumably stemming from the In_2S_3 precursor and/or sulfur-containing byproducts (eq 1). Table 1 summarizes the indium, nitrogen, and sulfur components of the InN NC samples as determined by EA and XPS. The In/S ratio does not significantly change when the OAm ligand is removed by Et_3OBF_4, but oxidation with $NOBF_4$ results in a drastic decrease (by >50%) in sulfur content relative to In. We believe that these data point to a system in which an optically inactive sulfur-rich shell withstands the ligand exchange step but is partially removed during oxidation with $NOBF_4$ (Figure 6).

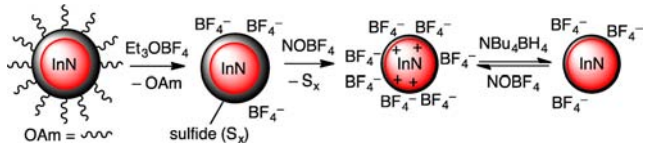

Figure 6. Depiction of the ligand removal process and partial removal of sulfur-rich shell followed by reversible oxidation and reduction of the InN core.

Given that reduction of oxidized InN NCs returns the original spectroscopic features of unoxidized (Et_3OBF_4-treated) NCs (Figure 4c,d), it would appear that the observed spectroscopic changes upon oxidation/reduction are attributable to the InN core and not the sulfur-rich shell.

Another important factor for applications that capitalize on the unique photophysics of this nanomaterial is the ability to not only modify but also to dynamically tune the LSPR. We found that oxidized InN NCs can be reduced using the mild reductant tetrabutylammonium borohydride (Bu_4NBH_4), with full recovery of the LSPR intensity and the original absorption onset position at ~1.8 eV (Figure 4d). Similar to those observed with the oxidation reaction, the optical properties are tuned in a stepwise fashion by adding increasing amounts of Bu_4NBH_4 (Figure 4d). The reversibility of the carrier density change suggests that redox only affects the optical properties of the InN core.

We explored further how the redox chemistry affects the properties of these InN NCs using FTIR absorbance spectroscopy. As shown in Figure 7, thin films of 6.0 ± 2.2 nm diameter OAm-capped InN NCs exhibit a LSPR absorbance maximum at 2996 nm that shifts to lower energy (3303 nm) in films prepared using InN NC treated with Et_3OBF_4. Given that the solution-phase data in Figure 4b show minimal changes to the absorption onset and LSPR intensity upon ligand exchange, it is unlikely that the carrier density is modified by ligand exchange, and thus, a different factor likely causes this shift. The FTIR data in Figure 7 also demonstrate that the OAm ligands are no longer present upon treatment with Et_3OBF_4 as evidenced by the elimination of aliphatic C–H

dx.doi.org/10.1021/ja404599g | J. Am. Chem. Soc. 2013, 135, 14142−14150

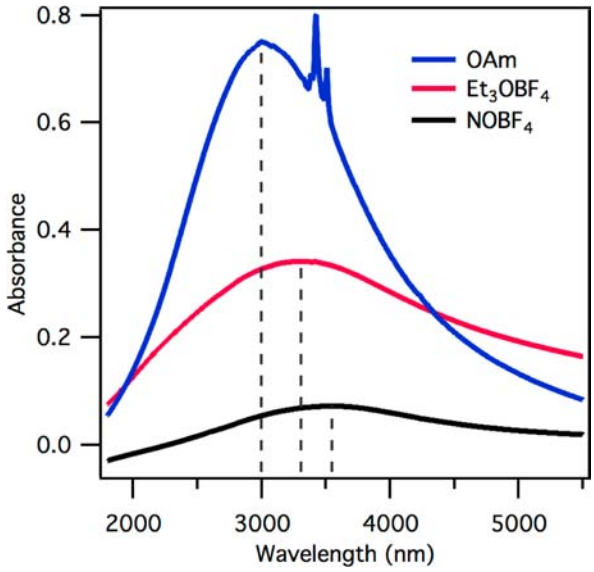

Figure 7. FTIR spectra of films of 6.0 ± 2.2 nm InN NCs with as-prepared OAm ligands (blue), following ligand exchange with Et_3OBF_4 (red) and upon oxidation with $NOBF_4$ (black).

stretching modes from 3400 to 3500 nm (~2900 cm^{-1}). This surface chemistry exchange results in a change in the dielectric medium for films of Et_3OBF_4-treated InN NCs from primarily organics (for the densely packed films made from OAm-capped NCs) to a combination of air, BF_4^- ligands, and other InN NCs. Therefore, we attribute this LSPR shift upon ligand exchange to a change in the dielectric environment surrounding the InN NCs, which is known to impact the LSPR energy (vide infra).[35,36] Once oxidized with $NOBF_4$, the LSPR absorbance maximum shifts to 3545 nm. Given the BF_4^- surface ligands in both samples, no major variations in the dielectric medium are expected, and we thus attribute the LSPR shift upon oxidation to a lower carrier density. Qualitatively, FTIR data of InN NC thin films made from oxidized InN NCs exhibit a lower intensity LSPR absorbance than those with OAm-capped or unoxidized, BF_4^--exchanged samples (Figure 7), consistent with the UV−vis−NIR data in Figure 4b. However, quantitative comparison of the LSPR intensity in films would require FTIR data from samples with identical film thicknesses and orientations. Since immersing an OAm-capped InN NC film in ACN solutions of Et_3OBF_4 or $NOBF_4$ desorbs the film from the substrate (owing to the solubility of BF_4^--capped NCs in ACN), a quantitative comparison was not possible.

Another method to gauge the effectiveness of chemical oxidation is to estimate the change in free carrier density of the InN NC samples from the LSPR frequency, which is commonly used to calculate carrier density in semiconductor nanocrystals.[28,33,35,36,38,41,54] Equation 1 was used to calculate the plasma frequency, ω_p, from the LSPR frequency, ω_{LSPR} (both in untis of cm^{-1}), with ε_∞ being the permittivity of free space and ε_m the high frequency dielectric constant of the material (6.7 for InN).[1,55] We ignore γ, the correction factor for inhomogeneity and scattering, because of the difficulty in estimating this term for NC samples as has been discussed elsewhere.[33]

$$\omega_p = \sqrt{(\varepsilon_\infty + 2\varepsilon_m)(\omega_{LSPR}{}^2 + \gamma^2)} \quad (1)$$

Free carrier density (N_{fc}) can be calculated from eq 2 using the plasma frequency (ω_p) derived from eq 1, where c is the speed of light, m_e^* is the free carrier effective mass ($m_e^*/m_0 = 1$), ε_0 is the dielectric of the surrounding medium, and e the charge of an electron.

$$N_{fc} = \frac{(2\pi c\omega_p)^2 m_e^* \varepsilon_0}{e^2} \quad (2)$$

The dielectric of the surrounding medium in solution is likely to be a combination of both the solvent (TCE, $\varepsilon_0 = 2.5$) and NC capping group (OAm,$\varepsilon_0 = 2.13$), with the effect of the ligand being more pronounced with smaller particle size.[56] The dielectric constant used for calculating the carrier density in this case was 2.3, assuming some contribution from both OAm and TCE, which gives a carrier density in as-synthesized OAm-capped InN NCs of 2.86 × 10^{20} cm^{-3}. For films of OAm-capped NCs, a carrier density of 2.89 × 10^{20} cm^{-3} was calculated using the dielectric of OAm (2.13) owing to the long (~2 nm) ligand length and good film density (i.e., containing minimal air). Because of the complexity of the dielectric environment surrounding BF_4^--capped NCs (comprising some combination of the dielectrics of air, BF_4^-, and InN), the dielectric for this medium was calculated based on the assumption that the carrier density was the same in films comprising OAm-capped and Et_3OBF_4-treated InN NCs. This assumption appears to be reasonable based on the similar absorption onsets and LSPR intensities for these two samples in the solution phase (Figure 4b). A dielectric constant of 5.45 is obtained when a carrier concentration of 2.89 × 10^{20} cm^{-3} and LSPR peak maximum of 3303 cm^{-1} are used in eq 2, consistent with the expected increase in dielectric for a medium with substantial contribution from close-neighbor InN NCs (dielectric of InN is 10.5).[1,54] This dielectric value was then used to calculate the carrier concentration of the film of $NOBF_4$-oxidized NCs under the assumption that the surrounding dielectric remains the same as the Et_3OBF_4-treated NCs. We used a constant electron effective mass of 0.15 based on experimental and theoretical electron effective masses found for carrier concentrations close to the 3 × 10^{20} cm^{-3} observed here.[1] Size and shape also play a role in the observed LSPR frequency,[40,57] but given that the same sample was used throughout this experiment, frequency changes due to changes in size and shape were ignored. Using these values and assumptions, oxidation with $NOBF_4$ reduces the carrier concentration by 3.8 × 10^{19} cm^{-3} (13%) to 2.51 × 10^{20} cm^{-3} (carrier density data summarized in Table S4). Given a NC diameter of 6 nm containing approximately 5000 atoms and having a volume of ~1 × 10^{-19} cm^3, this value corresponds to the removal of 4 electrons per InN NC via chemical oxidation with excess $NOBF_4$.

4. CONCLUSIONS

In this work, we have demonstrated the ability to control the average size of InN NCs (4−10 nm) with polydispersities of <20% via size-selective precipitation. As-prepared InN NCs exhibit an absorption onset at ~1.8 eV along with a strong LSPR feature in the IR region centered near 3000 nm. The significantly higher energy absorption onset compared to the expected band gap of bulk InN (~0.7 eV) is due to an excess of charge carriers resulting in a Burstein−Moss shift. Surface chemistry treatment using Et_3OBF_4 is shown to exchange the capping ligands from OAm to BF_4^- and result in polar solvent-soluble InN NCs. Chemical oxidation of these species with $NOBF_4$ is found to red-shift the absorption onset to ~1.3 eV

and reduce the plasmon absorption energy (from 3303 to 3545 nm) and intensity (by an order of magnitude at 2600 nm), all of which are fully reversible via reduction with Bu_4NBH_4 over these ranges. The calculated carrier density in these InN NCs decreases from 2.89×10^{20} cm^{-3} to 2.51×10^{20} cm^{-3} upon oxidation consistent with the removal of ∼4 electrons per NC. This study provides a unique example of the ability to tune the optical properties of colloidal nanomaterials, and in particular the LSPR absorption, with reversible redox reactions that do not affect the semiconductor chemical composition or phase. Additional tuning of the carrier density to push the Fermi level below that of the conduction band minimum will facilitate exploration of the quantum confinement behavior of InN NCs for advanced optoelectronics applications such as hot carrier and multiple exciton generation-based photovoltaics.

■ ASSOCIATED CONTENT

Supporting Information

InN NC formation mechanistic discussion; size histogram of size-selected InN NCs; XRD spectra, TEM images, size histograms, and summary table of products at varied reaction times; XRD spectra, TEM images, size histograms, and summary table of products at varied reaction temperatures; XRD spectra of products from reactions with varying In/N ratios; XRD spectra of OAm- and $NOBF_4$-oxidized InN NCs; table of carrier concentration calculation results; EA and XPS data for F and B, XPS survey spectra and high resolution spectra of In, N, and P regions. This material is available free of charge via the Internet at http://pubs.acs.org.

■ AUTHOR INFORMATION

Corresponding Author

Nathan.Neale@nrel.gov

Notes

The authors declare no competing financial interest.

■ ACKNOWLEDGMENTS

The authors thank Jao van de Lagemaat (NREL), Joseph M. Luther (NREL), Delia J. Milliron (LBNL), and Craig L. Perkins (NREL) for helpful discussions. X-ray photoelectron spectroscopy was funded by the NREL LDRD Director's Fellowship Program. All other aspects of this work were supported by the Solar Photochemistry Program of the Division of Chemical Sciences, Geosciences, and Biosciences, Office of Basic Energy Sciences of the U.S. Department of Energy through Grant DE-AC36-08GO28308 to NREL.

■ REFERENCES

(1) Wu, J. *J. Appl. Phys.* **2009**, *106*, 011101.
(2) Walukiewicz, W.; Ager, J. W., III; Yu, K. M.; Liliental-Weber, Z.; Wu, J.; Li, S. X.; Jones, R. E.; Denlinger, J. D. *J. Phys. D: Appl. Phys.* **2006**, *39*, R83.
(3) Bhuiyan, A. G.; Hashimoto, A.; Yamamoto, A. *J. Appl. Phys.* **2003**, *94*, 2779−2808.
(4) Wu, J.; Walukiewicz, W.; Yu, K. M.; Ager, J. W., III; Haller, E. E.; Lu, H.; Schaff, W. J.; Saito, Y.; Nanishi, Y. *Appl. Phys. Lett.* **2002**, *80*, 3967−3969.
(5) Liu, C.; Li, J. *Phys. Lett. A* **2011**, *375*, 1152−1155.
(6) Monemar, B.; Paskov, P. P.; Kasic, A. *Superlattices Microstruct.* **2005**, *38*, 38−56.
(7) Wu, J.; Walukiewicz, W.; Li, S. X.; Armitage, R.; Ho, J. C.; Weber, E. R.; Haller, E. E.; Lu, H.; Schaff, W. J.; Barcz, A.; Jakiela, R. *Appl. Phys. Lett.* **2004**, *84*, 2805−2807.
(8) McLaughlin, D. V. P.; Pearce, J. M. *Metall. Mater. Trans. A* **2013**, *44A*, 1947−1954.
(9) Feng, Y.; Aliberti, P.; Veettil, B. P.; Patterson, R.; Shrestha, S.; Green, M. A.; Conibeer, G. *Appl. Phys. Lett.* **2012**, *100*, 053502.
(10) Jensen, S. A.; Versluis, J.; Canovas, E.; Pijpers, J. J. H.; Sellers, I. R.; Bonn, M. *Appl. Phys. Lett.* **2012**, *101*, 222113.
(11) Chen, F.; Cartwright, A. N.; Lu, H.; Schaff, W. J. *Appl. Phys. Lett.* **2003**, *83*, 4984−4986.
(12) Mahboob, I.; Veal, T. D.; McConville, C. F.; Lu, H.; Schaff, W. J. *Phys. Rev. Lett.* **2004**, *92*, 036804.
(13) King, P. D. C.; Veal, T. D.; McConville, C. F.; Fuchs, F.; Furthmuller, J.; Bechstedt, F.; Schley, P.; Goldhahn, R.; Schormann, J.; As, D. J.; Lischka, K.; Muto, D.; Naoi, H.; Nanishi, Y.; Lu, H.; Schaff, W. J. *Appl. Phys. Lett.* **2007**, *91*, 092101.
(14) Walukiewicz, W.; Li, S. X.; Wu, J.; Yu, K. M.; Ager, J. W., III; Haller, E. E.; Lu, H.; Schaff, W. J. *J. Cryst. Growth* **2004**, *269*, 119−127.
(15) Dixit, A.; Sudakar, C.; Thakur, J. S.; Padmanabhan, K.; Kumar, S.; Naik, R.; Naik, V. M.; Lawes, G. *J. Appl. Phys.* **2009**, *105*, 053104.
(16) Atwater, H. A.; Polman, A. *Nat. Mater.* **2010**, *9*, 205−213.
(17) Mokari, T.; Rothenberg, E.; Popov, I.; Costi, R.; Banin, U. *Science* **2004**, *304*, 1787−1790.
(18) Zhang, W.; Govorov, A. O.; Bryant, G. W. *Phys. Rev. Lett.* **2006**, *97*, 146804.
(19) Govorov, A. O.; Bryant, G. W.; Zhang, W.; Skeini, T.; Lee, J.; Kotov, N. A.; Slocik, J. M.; Naik, R. R. *Nano Lett.* **2006**, *6*, 984−994.
(20) Berr, M.; Vaneski, A.; Susha, A. S.; Rodriguez-Fernandez, J.; Doblinger, M.; Jackel, F.; Rogach, A. L.; Feldmann, J. *Appl. Phys. Lett.* **2010**, *97*, 093108-3.
(21) Xiao, J.; Xie, Y.; Tang, R.; Luo, W. *Inorg. Chem.* **2002**, *42*, 107−111.
(22) Schofield, P. S.; Zhou, W.; Wood, P.; Samuel, I. D. W.; Cole-Hamilton, D. J. *J. Mater. Chem.* **2004**, *14*, 3124−3126.
(23) Sardar, K.; Deepak, F. L.; Govindaraj, A.; Seikh, M. M.; Rao, C. N. R. *Small* **2005**, *1*, 91−94.
(24) Wu, C.; Li, T.; Lei, L.; Hu, S.; Liu, Y.; Xie, Y. *New J. Chem.* **2005**, *29*, 1610−1615.
(25) Choi, J.; Gillan, E. G. *J. Mater. Chem.* **2006**, *16*, 3774−3784.
(26) Hsieh, J. C.; Yun, D. S.; Hu, E.; Belcher, A. M. *J. Mater. Chem.* **2010**, *20*, 1435−1437.
(27) Chen, Z.; Li, Y.; Cao, C.; Zhao, S.; Fathololoumi, S.; Mi, Z.; Xu, X. *J. Am. Chem. Soc.* **2011**, *134*, 780−783.
(28) Garcia, G.; Buonsanti, R.; Runnerstrom, E. L.; Mendelsberg, R. J.; Llordes, A.; Anders, A.; Richardson, T. J.; Milliron, D. J. *Nano Lett.* **2011**, *11*, 4415−4420.
(29) Kanehara, M.; Koike, H.; Yoshinaga, T.; Teranishi, T. *J. Am. Chem. Soc.* **2009**, *131*, 17736−17737.
(30) Buonsanti, R.; Llordes, A.; Aloni, S.; Helms, B. A.; Milliron, D. J. *Nano Lett.* **2011**, *11* (11), 4706−4710.
(31) Schimpf, A. M.; Ochsenbein, S. T.; Buonsanti, R.; Milliron, D. J.; Gamelin, D. R. *Chem. Commun.* **2012**, *48*, 9352−9354.
(32) Manthiram, K.; Alivisatos, A. P. *J. Am. Chem. Soc.* **2012**, *134*, 3995−3998.
(33) Rowe, D. J.; Jeong, J. S.; Mkhoyan, K. A.; Kortshagen, U. R. *Nano Lett.* **2013**, *13*, 1317−1322.
(34) Wehrenberg, B. L.; Guyot-Sionnest, P. *J. Am. Chem. Soc.* **2003**, *125*, 7806−7807.
(35) Luther, J. M.; Jain, P. K.; Ewers, T.; Alivisatos, P. A. *Nat. Mater.* **2011**, *10*, 361−366.
(36) Kriegel, I.; Jiang, C.; Rodríguez-Fernández, J.; Schaller, R. D.; Talapin, D. V.; da Como, E.; Feldmann, J. *J. Am. Chem. Soc.* **2011**, *134*, 1583−1590.
(37) Dorfs, D.; Härtling, T.; Miszta, K.; Bigall, N. C.; Kim, M. R.; Genovese, A.; Falqui, A.; Povia, M.; Manna, L. *J. Am. Chem. Soc.* **2011**, *133*, 11175−11180.
(38) Zhao, Y.; Pan, H.; Lou, Y.; Qiu, X.; Zhu, J.; Burda, C. *J. Am. Chem. Soc.* **2009**, *131*, 4253−4261.
(39) Hsu, S.-W.; Bryks, W.; Tao, A. R. *Chem. Mater.* **2012**, *24*, 3765−3771.

(40) Niezgoda, J. S.; Harrison, M. A.; McBride, J. R.; Rosenthal, S. J. *Chem. Mater.* **2012**, *24*, 3294−3298.
(41) Routzahn, A. L.; White, S. L.; Fong, L.-K.; Jain, P. K. *Isr. J. Chem.* **2012**, *52*, 983−991.
(42) Perkins, C. L.; Hasoon, F. S. *J. Vac. Sci. Technol., A* **2006**, *24* (3), 497−504.
(43) Purdy, A. P. *Inorg. Chem.* **1994**, *33*, 282−286.
(44) John, S.; Soukoulis, C.; Cohen, M. H.; Economou, E. N. *Phys. Rev. Lett.* **1986**, *57*, 1777−1780.
(45) Butcher, K. S. A.; Hirshy, H.; Perks, R. M.; Wintrebert-Fouquet, M.; Chen, P. P. T. *Phys. Status Solidi A* **2006**, *203*, 66−74.
(46) Rosen, E. L.; Buonsanti, R.; Llordes, A.; Sawvel, A. M.; Milliron, D. J.; Helms, B. A. *Angew. Chem., Int. Ed.* **2012**, *51* (3), 684−689.
(47) Connelly, N. G.; Geiger, W. E. *Chem. Rev.* **1996**, *96*, 877−910.
(48) Dong, A.; Ye, X.; Chen, J.; Kang, Y.; Gordon, T.; Kikkawa, J. M.; Murray, C. B. *J. Am. Chem. Soc.* **2010**, *133*, 998−1006.
(49) Dabbousi, B. O.; Rodriguez-Viejo, J.; Mikulec, F. V.; Heine, J. R.; Mattoussi, H.; Ober, R.; Jensen, K. F.; Bawendi, M. G. *J. Phys. Chem. B* **1997**, *101*, 9463−9475.
(50) Moreels, I.; Lambert, K.; De Muynck, D.; Vanhaecke, F.; Poelman, D.; Martins, J. C.; Allan, G.; Hens, Z. *Chem. Mater.* **2007**, *19*, 6101−6106.
(51) Jasieniak, J.; Mulvaney, P. *J. Am. Chem. Soc.* **2007**, *129*, 2841−2848.
(52) Cossairt, B. M.; Juhas, P.; Billinge, S. J. L.; Owen, J. S. *Phys. Chem. Lett.* **2011**, *2*, 3075−3080.
(53) Hughes, B. K.; Ruddy, D. A.; Blackburn, J. L.; Smith, D. K.; Bergren, M. R.; Nozik, A. J.; Johnson, J. C.; Beard, M. C. *ACS Nano* **2012**, *6*, 5498−5506.
(54) Mulvaney, P. *Langmuir* **1996**, *12*, 788−800.
(55) Inushima, T.; Higashiwaki, M.; Matsui, T. *Phys. Rev. B* **2003**, *68*, 235204.
(56) Templeton, A. C.; Pietron, J. J.; Murray, R. W.; Mulvaney, P. *J. Phys. Chem. B* **1999**, *104*, 564−570.
(57) Lu, X.; Rycenga, M.; Skrabalak, S. E.; Wiley, B.; Xia, Y. *Annu. Rev. Phys. Chem.* **2009**, *60*, 167−192.